Inorganic Chemistry

pubs.acs.org/IC Article

Bis-Alkynyl Complexes of Fe(III) Tetraaza Macrocycles—A Tale of Two Rings

Reese A. Clendening, Matthias Zeller, and Tong Ren*

Cite This: *Inorg. Chem.* 2022, 61, 13442−13452 Read Online

ACCESS | Metrics & More | Article Recommendations | Supporting Information

ABSTRACT: Reported herein are new Fe bis-alkynyl complexes $[Fe^{III}(L)(C_2R)_2]BPh_4$ based on tetra*imine* macrocycle (L = HMTI = *meso*-5,5,7,12,12,14-hexamethyl-1,4,8,11-tetraazacyclotetradeca-1,3,8,10-tetraene; **1a**−**1c**; R = C_6H_5 (**a**), $C_{10}H_9$ (**b**), $SiMe_3$ (**c**)) and tetra*amine* macrocycle (L = HMC = *meso*-5,5,7,12,12,14-hexamethyl-1,4,8,11-tetraazacyclotetradecane; **2a**−**2c**). These complexes have been characterized using single-crystal X-ray diffraction, electronic absorption spectroscopy, and cyclic and differential pulse voltammetry. Spectroelectrochemical studies of **1a** and **2a** allowed for investigation of the Fe^{II} oxidation state, which revealed a strong dependence on the nature of the macrocycle for both the energies of the Fe^{II} to C_2Ph metal-to-ligand charge transfer (MLCT) and the $\nu(C{\equiv}C)$. The $\nu(C{\equiv}C)$ was further influenced by the oxidation state, though sensitivity to the formal metal oxidation state was much higher in the case of **2a** than in **1a**. These findings are rationalized on the basis of the relative energies of the formally metal-centered orbitals *via* density functional theory calculations.

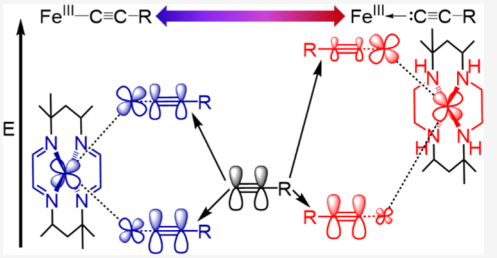

INTRODUCTION

Metal alkynyls have long enjoyed considerable interest over a wide range of topics.[1−3] In particular, the structural rigidity of C_{2n} groups and their ability to engage in π interactions with both metal dπ and aryl π-orbitals have resulted in the widespread use of metal-alkynyl complexes for studies of mixed valency,[4−6] photovoltaic materials,[7,8] nonlinear optical materials,[9,10] and molecular electronic devices.[11,12] Overall, the tunability of alkynyl complexes in achieving desired properties has been demonstrated through the efforts of many laboratories[1,2,13−18] during the decades since the pioneering work of Nast.[19]

Ru-alkynyl compounds have played key roles in both synthetic method development of metal alkynyls and demonstration of extensive conjugation along Ru-alkynyl backbones.[1,2,20,21] Facile electron delocalization both through an oligoyn-diyl between two Ru centers[22,23] and across a -C_2-Ru-C_2- unit[24] has been demonstrated *via* the mixed valency therein. The excellence of Ru alkynyls in mediating charge transfer has been further validated using single-molecule measurement.[25−28] The demonstration of Ru−Ru long-distance coupling through oligothienylethynyl bridges by Patra and co-workers is an interesting recent development.[29,30] The majority of the aforementioned Ru alkynyls are supported with soft ligands such as phosphines and cyclopentadienyls (Cp/Cp*). It is noteworthy that Che and co-workers demonstrated significant conjugation in Ru alkynyls supported with a saturated tetraaza macrocycle—a *hard* ligand.[31]

While many of the aforementioned applications have been achieved with 4d and 5d metals, sustainability considerations command the pursuit of complexes based on less toxic and/or more readily available elements.[32] The feasibility of realizing extensive π conjugation with 3d metals was illustrated with compounds of Fe, the group 8 congener of Ru, which consisted of oligoyn-diyls capped with $Cp^*Fe^{II}(P\text{-}P)$ by Lapinte and co-workers (type **I** in Chart 1)[33] and subsequently with

Chart 1. Illustration of Common Supporting Ligand Motifs (I−V) for Iron-alkynyl Complexes

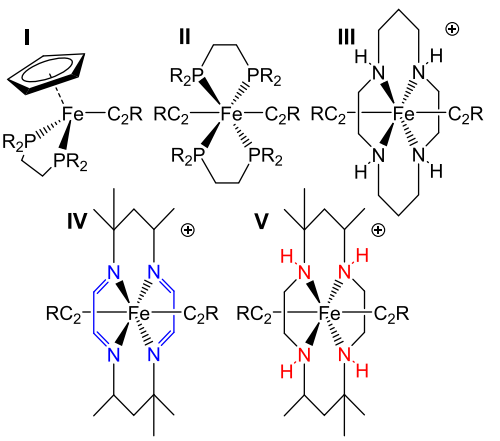

Received: May 20, 2022
Published: August 2, 2022

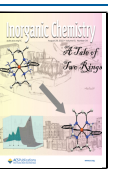

https://doi.org/10.1021/acs.inorgchem.2c01743
Inorg. Chem. 2022, 61, 13442−13452

$Cp^*Fe(CO)_2$ by Akita and co-workers.[34] Since then, the degree of π-conjugation between Cp^*Fe^{II}(P-P) and hydrocarbon ligands has been explored extensively by Lapinte and co-workers.[4,6,35] More recently, significant electronic conduction across Fe-C_{2n}-Fe motifs has been demonstrated with the $Fe^{II}(P\text{-}P)_2$ type building blocks (Chart 1, **II**).[36,37] Similar to the cases of Ru, all of the aforementioned Fe-alkynyl examples involve soft auxiliary ligands such as Cp/Cp*, CO, and phosphines.

There has been a continued interest in supporting 3d metal-alkynyl complexes with polyaza macrocycles, including Cr^{III} species supported with Me_3TACN (trimethyl-1,4,7-triazacyclononane) and cyclam (1,4,8,11-tetraazacyclotetradecane) by Berben and Long,[38,39] Cr^{III} and Co^{III} species with cyclam by Wagenknecht and co-workers,[40,41] and Co^{III}(cyclam) species by Shores and co-workers.[42,43] Our laboratory has broadly explored the chemistry of 3d metal alkynyls supported with both cyclam and its *C*-substituted derivatives in recent years.[44,45] In particular, Fe^{III}(cyclam) complexes bearing both simple alkynyls (C_2R; Chart 1, **III**) and *gem*-diethynylethene were investigated.[46−48] The π-conjugation in the Fe-alkynyl backbone was unremarkable in these Fe^{III} complexes, which is likely attributed to the *hard* base nature of cyclam, a saturated tetraaza macrocycle. Here, we report two series of related Fe^{III} bis-alkynyls based on HMTI (*meso*-5,5,7,12,12,14-hexamethyl-1,4,8,11-tetraazacyclotetradeca-1,3,8,10-tetraene; Chart 1, **IV**) and HMC (*meso*-5,5,7,12,12,14-hexamethyl-1,4,8,11-tetraazacyclotetradecane; Chart 1, **V**). In addition to characterizations with X-ray diffraction and routine voltammetric techniques, the Vis−NIR and IR spectroelectrochemical (SEC) responses in both types **IV** and **V** complexes were carefully analyzed and corroborated with TD-DFT analysis to gain insight into the impact of ring unsaturation on the electronic structures, especially the enhancement of π-conjugation in the former.

Scheme 1. Synthesis of 1a−1c and 2a−2c. (i) Excess LiC_2R, −78 to 0 °C under N_2; (ii) O_2, Methanol, $NaBPh_4$; (iii) Purification through Silica (1a, 1c) or Celite (1b); (iv) Excess LiC_2R, −78 to 0 °C (−78 °C to r.t. for 2a) under N_2; $NaBPh_4$; and (v) Filtration through Silica (2a, 2c) or Celite (2b) under Ambient Conditions

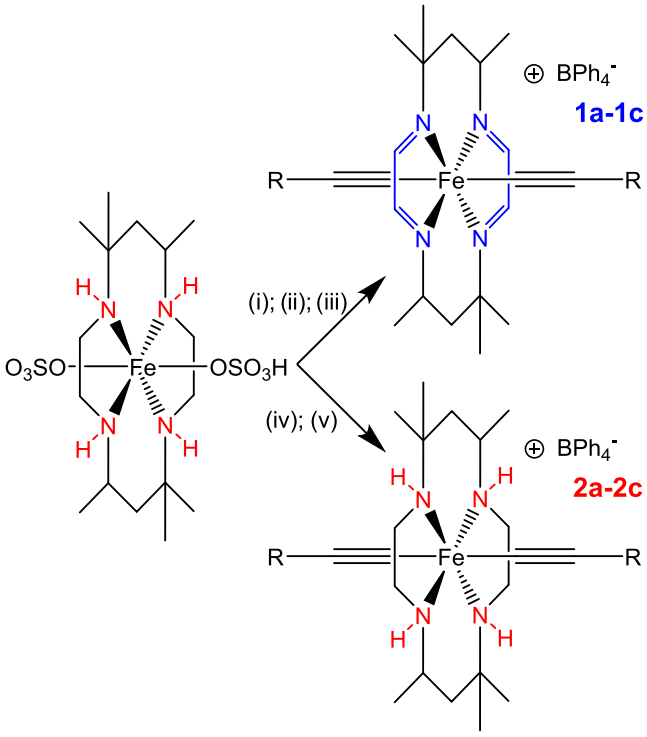

R = phenyl (Ph, **1a/2a**); 1-naphthyl (Np, **1b/2b**) and trimethylsilyl ($SiMe_3$, **1c/2c**)

RESULTS AND DISCUSSION

Synthesis. The new compound $Fe^{III}(HMC)(SO_4)(HSO_4)$ was obtained from the mixing of hot methanolic solutions of HMC and $Fe(SO_4)_2{\cdot}7H_2O$, followed by the addition of excess sulfuric acid in the presence of oxygen. The product precipitated from the crude solution and was isolated by filtration in moderate yields (*ca.* 50%).

Similar to the recently reported $[Fe(HMTI)(C_2SiEt_3)_2]ClO_4$ (**1d**),[49] complexes **1a−1c** were synthesized by the addition of the lithiated alkyne (excess) to $Fe(HMC)(SO_4)(HSO_4)$ at low temperature, as shown in Scheme 1. The reaction mixture was then exposed to air with the addition of a few drops of methanol, followed by briefly bubbling oxygen through the solution. Sodium tetraphenylborate ($NaBPh_4$) was added in excess, and the mixture was crudely purified over Celite and/or silica. The oxidizing conditions result in the *in situ* oxidative dehydrogenation of the supporting macrocycle HMC to result in the corresponding tetra*imine* complex.[50] Following careful purification over silica, $[Fe(HMTI)(C_2Ph)_2](BPh_4)$ (**1a**), $[Fe(HMTI)(C_2Np)_2](BPh_4)$ (Np = 1-naphthyl, **1b**), and $[Fe(HMTI)(C_2SiMe_3)_2](BPh_4)$ (**1c**) are obtained in poor to moderate yields (13−26%).

Complexes **2a−2c** were similarly synthesized by the addition of an excess of lithiated alkyne to $Fe(HMC)(SO_4)(HSO_4)$ at low temperature, as shown in Scheme 1. However, moisture and oxygen were excluded prior to the addition of $NaBPh_4$, which was followed by rapid filtration through Celite and/or silica. This process generates the symmetrical alkynyl derivatives $[Fe(HMC)(C_2Ph)_2](BPh_4)$ (**2a**), $[Fe(HMC)(C_2Np)_2](BPh_4)$ (**2b**), and $[Fe(HMC)(C_2SiMe_3)_2](BPh_4)$ (**2c**), again in low to moderate yields (11−33%).

Both series of complexes appear to be stable as solids and may be readily handled in the presence of oxygen once isolated. No conversion of **2a−2c** into their respective dehydrogenated counterparts has been observed once isolated, suggesting that the combination of oxygen and a strong base (*i.e.*, CH_3O^- generated by quenching the excess lithium-alkyl/alkynyl reagents) is necessary to promote oxidative dehydrogenation. Despite the stability of both series toward ambient conditions, the generally low yields (≤33%) are currently not well understood. Spectroelectrochemistry on **2a** (*vide infra*) suggests that the stability of $Fe^{II}(HMC)(C_2Ph)_2$ is modest; therefore, the low yields may be due to the partial decomposition of the $Fe^{II}(HMC)(C_2R)_2$ intermediates.

The compositions of all new complexes have been confirmed with both ESI-MS and elemental analysis. Room temperature effective magnetic moments (Supporting Information [SI], Table S1) of both series **1** and **2** by Evans method[51] range between 3.0 and 4.3 Bohr magneton (μ_B), higher than the expected value for an $S = 1/2$ species (1.73 μ_B).

Structural Characterization. Single crystals suitable for X-ray diffraction were obtained for all complexes except **1b**. Crystals of **1a** were quite small, resulting in rather low-resolution structural data. However, the $CF_3SO_3^-$ salt of **1a** (hereafter **1a-OTf**) yielded better diffracting crystals and much

https://doi.org/10.1021/acs.inorgchem.2c01743
Inorg. Chem. 2022, 61, 13442−13452

higher precision data. The structures of **1a** and Fe(HMC)-$(SO_4)_2(H_5O_2)$ are shown in Figures S1 and S2, while the cationic portions of the remaining structures are shown in Figure 1. All structures exhibit a pseudo-octahedral geometry

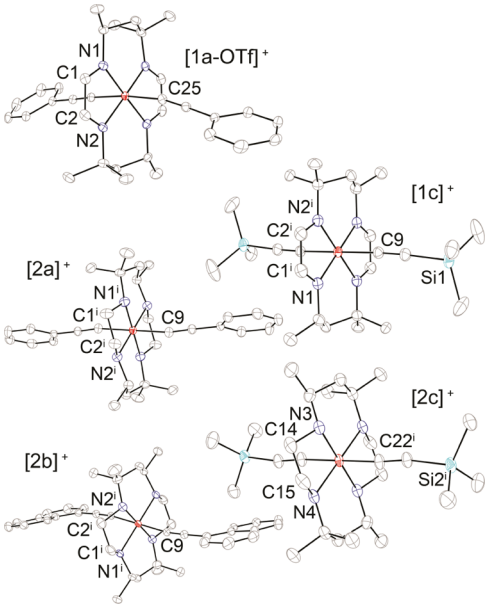

Figure 1. ORTEP plots of $[\mathbf{1a\text{-}OTf}]^+$, $[\mathbf{1c}]^+$, and $[\mathbf{2a}]^+$–$[\mathbf{2c}]^+$ at the 30% probability level. Hydrogen atoms, solvate, disorder, counteranions, and additional independent cations are omitted for clarity.

around the Fe center, with the macrocyclic nitrogens occupying the equatorial plane and the axial alkynyls being *trans* to each other. The linear coordination of the alkynyls is confirmed by examining the Fe-C≡C angles, all of which are >169°. Moreover, the C≡C bond lengths are consistent with carbon–carbon triple bonds, ranging from 1.207(2) to 1.220(2) Å.[16,17] These parameters agree very well with those reported for other bis-alkynyl species.[47,49,52]

Importantly, the structural parameters highlight the conversion of HMC to HMTI through oxidative dehydrogenation. Within the N=C-C=N moiety, the nitrogen–carbon bonds of **1a-OTf** and **1c** are consistent with a double-bond assignment (1.280(3)-1.286(3) Å), while the carbon–-carbon bonds are longer (1.432(3)–1.442(3) Å; Table 1). This portion of the chelate ring is planar, with dihedral angles under 2° in all cases. In contrast, the related N-C (1.421(4)–1.485(3) Å) and C-C (1.493(4)–1.511(4) Å) bond lengths of **2a**–**2c** are indicative of single bonds. The saturated HMC is much more flexible, with the analogous N-C-C-N dihedral angles between 50 and 59°. Together, these bond metrics support the α-diimine assignment for **1a**–**1c**, although the *ca.* 0.06 Å contraction of the C-C bond in **1a-OTf**/**1c** versus **2a**/**2c** points to some π delocalization within the α-diimine unit.

As expected from the previous analysis of **1d**,[49] the Fe-N bond lengths of **1a-OTf** and **1c** (1.926(1)–1.938(1) Å) are short compared to those of **2a**–**2c** (2.012(2)–2.046(4) Å). The latter are only slightly elongated compared to the Fe-N bonds of analogous Fe^{III}(cyclam) species (1.999(4)–2.013(2)Å), consistent with the steric contribution of the macrocyclic methyl groups.[47] The contraction of Fe-N bond lengths, *ca.* 0.1 Å, is consistent with the presence of Fe-π(α-diimine) interactions in addition to Fe-N σ bonding, signifying a departure from the σ-only Fe-N interactions in Fe(HMC) species. For **1a**, **1c**, and **1d**,[49] the Fe center is constrained to be coplanar with the nitrogen atoms by crystallographic symmetry. Though lacking an exact center of inversion, the Fe center in **1a-OTf** deviates from the mean plane of the four nitrogens by only 0.009 Å, similar to the previously published $[Fe^{II}(HMTI)(NCCH_3)(C_2SiEt_3)]^+$.[49]

The flattening of the macrocycle imposed by the α-diimine moieties appears to shorten the Fe-C bonds in tetraimine complexes **1a-OTf** (1.945(2), 1.949(2) Å) and **1c** (1.941(2), 1.951(2) Å) from those of HMC complexes **2a** (1.961(3), 1.962(3) Å) and **2c** (1.955(2), 1.959(2) Å). The difference, though small, is reproduced in the optimized geometries for each pair of complexes (*ca.* 0.02 Å calculated contraction, see Table S5). This may signal a slight increase in the metal-alkynyl bond strength for complexes of HMTI—a tentative interpretation that gains support from trends in the ν(C≡C) for **1**–**2** (see Figure S4) and spectroelectrochemical data (*vide infra*).

Electrochemistry. To interrogate the electronic influence of the supporting macrocycles, cyclic (CV) and differential pulse voltammograms (DPV) were measured for all complexes (Figure 2). All species exhibit irreversible oxidation (**B**) that is attributed to the oxidation of the tetraphenylborate counteranion,[53] which is absent in the CV of **1a-OTf**. Complexes of HMC (**2a**–**2c**) exhibit pseudo-reversible one-electron oxidations (**A**) assigned as an $Fe^{IV/III}$ event (confirmed *via* spectroelectrochemistry, *vide infra*). In comparison, the $Fe^{IV/III}$ couple was observed for $Fe(dmpe)_2(C_2Ph)_2$ (dmpe = 1,2-bis(dimethylphosphino)ethane) at 0.5 V vs ferrocene (Fc) in acetonitrile.[54] The reversible event **C** in each case is assigned to the $Fe^{III/II}$ reduction. An irreversible reduction (**D**), which only appears in **1a**–**1c**, is assigned to the reduction of the HMTI ligand.[49,55,56] Potentials for these events are given in Table 2.

Several significant contrasts between the voltammograms of series **1** and **2** are clear from Figure 2. The oxidation couple **A** appears only in the latter and is well-behaved in **2a** and **2b** with

Table 1. Selected Bond Lengths (Å) and Angles (deg)[a] for $[\mathbf{1a\text{-}OTf}]^+$, $[\mathbf{1c}]^+$, and $[\mathbf{2a}]^+$–$[\mathbf{2c}]^+$[b]

	$[\mathbf{1a\text{-}OTf}]^+$	$[\mathbf{1c}]^+$	$[\mathbf{2a}]^+$	$[\mathbf{2b}]^+$	$[\mathbf{2c}]^+$
Fe-C	1.945(2)–1.949(2)	1.941(2)–1.951(2)	1.961(3)–1.962(3)	1.984(4)–1.989(5)	1.955(2)–1.959(2)
Fe-N	1.926(1)–1.938(1)	1.932(2)–1.937(2)	2.012(2)–2.032(2)	2.014(2)–2.046(4)	2.020(2)–2.046(3)
N-C[c]	1.282(2)–1.286(2)	1.280(3)–1.286(3)	1.421(4)–1.470(4)	1.470(6)–1.485(3)	1.481(5)–1.485(3)
C-C[c]	1.442(3)	1.432(3)–1.434(3)	1.493(4)–1.497(4)	1.502(6)–1.511(4)	1.503(6)–1.504(4)
|N-C-C-N|	0.3(2)–0.6(2)	1.2(3)–1.9(3)	50.4(4)–53.3(3)	56.9(6)–57.8(3)	58.8(7)–57.1(3)

[a]Ranges are given to show the level of variation due merely to packing effects or experimental errors versus that which is inherent to the molecular structures. [b]For parameters affected by disorder, only the major disordered moiety was considered. [c]The C-C and N-C bonds refer to those within the N-C-C-N portion of the macrocycle.

https://doi.org/10.1021/acs.inorgchem.2c01743
Inorg. Chem. 2022, 61, 13442–13452

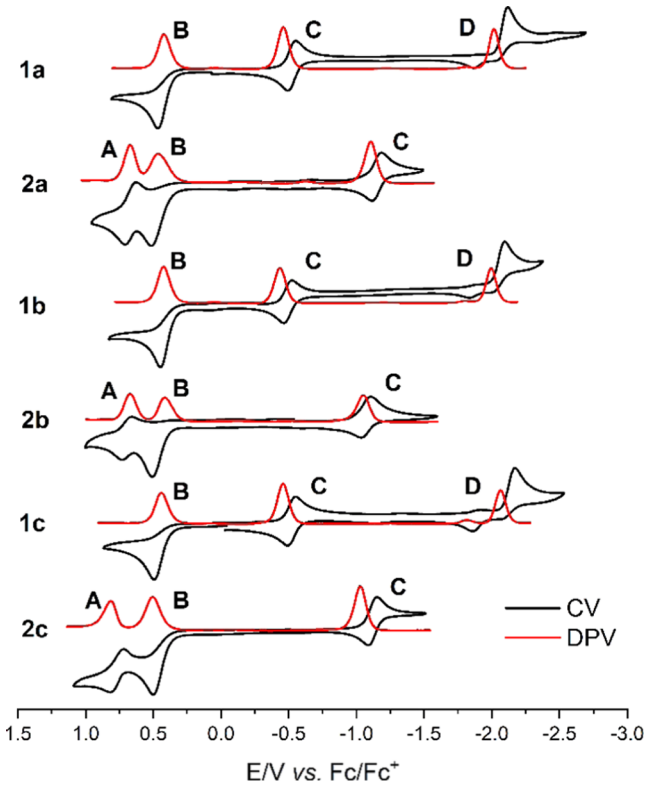

Figure 2. CV (0.1 V/s scan rate) and DPV traces of 1 mM solutions of **1a−1c** and **2a−2c** in acetonitrile (0.1 M NBu_4PF_6).

Table 2. Electrochemical Potentials (V vs Fc/Fc^+) of Selected Events for Complexes 1 and 2

	$E_{1/2}$(A)	$E_{1/2}$(C)	E_{pc}(D)
1a		-0.52	−2.12
2a	0.67	−1.15	
1b		−0.49	−2.09
2b	0.69	−1.07	
1c		−0.52	−2.17
2c	0.77	−1.12	

ΔE_p values of 65 and 71 mV, respectively,[57] while that of **2c** is less than ideal and occurs at an unexpectedly high potential (0.77 V). The strong donating nature of alkynyls clearly renders the Fe^{IV} state accessible, in contrast to the voltammetric behavior of the bis-acetonitrile complex $[Fe(HMC)(NCCH_3)_2]^{2+}$.[58] The lack of an $Fe^{IV/III}$ oxidation in **1a−1c** is attributed to the electron deficiency at the Fe center due to the strong electron-withdrawing nature of the dual α-diimine units in the HMTI macrocycle. The enhanced electron deficiency further manifests as a *ca.* 600 mV anodic shift in the iron-centered reductions (**C**) in series **1** from those in series **2**. The $Fe^{III/II}$ couple was observed at −0.59 V in acetonitrile for $Fe(dmpe)_2(C_2Ph)_2$,[54] indicating that HMTI stabilizes the neutral Fe^{II} complex slightly more than does the pair of bidentate phosphine chelators. These considerations are further corroborated by the SEC studies below. The irreversible reduction (**D**) in **1a−1c** is assigned to the redox-active HMTI ligand itself, as **2a−2c** lack any cathodic events past reduction **C**. Both $[Fe(HMTI)(NCCH_3)_2]^{2+}$ and $[Fe(HMTI)(NCCH_3)(C_2SiEt_3)]^+$ exhibit reversible macrocyclic reductions in acetonitrile solution, likely enabled by the fast exchange of coordinated acetonitrile.[49,58] The irreversibility of **D** in **1a−1c** may be due to the loss of one of the two alkynyl ligands.

Electronic Absorption Spectra. Further insight into the electronic structures of **1** and **2** may be gleaned from their electronic absorption spectra, which are dominated by intense, ligand-to-metal charge transfer (LMCT) bands in the Vis−NIR window (Figure 3). LMCT from alkynyl ligands to an

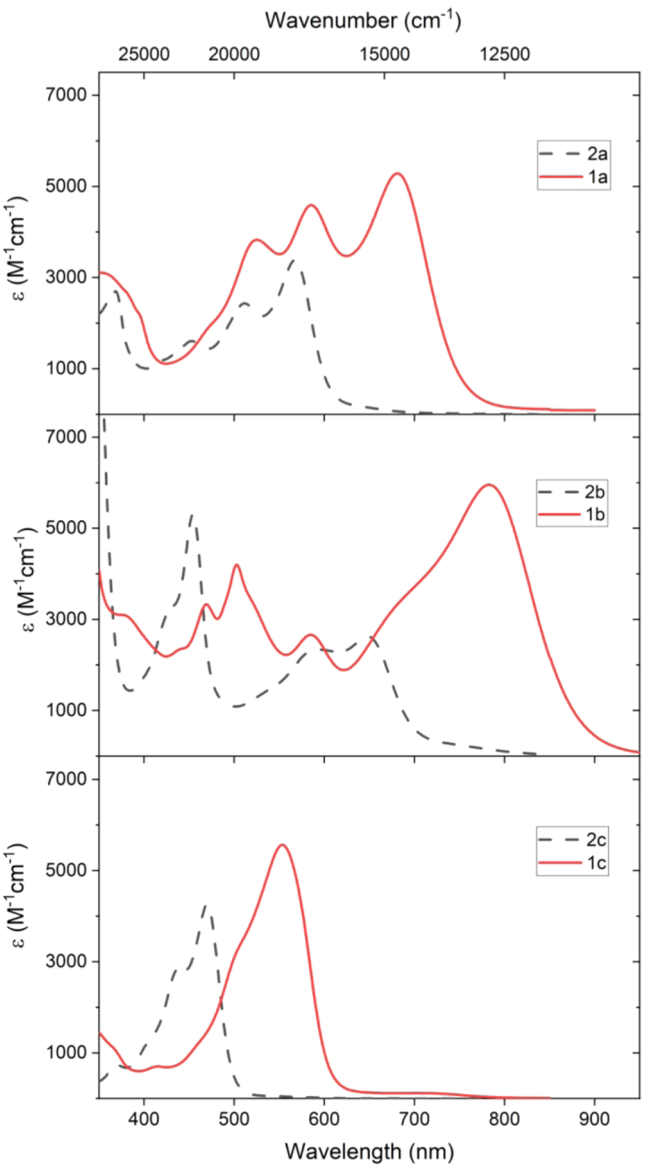

Figure 3. Electronic absorption spectra of **1**/**2a** (top), **1**/**2b** (middle), and **1**/**2c** (bottom) in acetonitrile; molar absorptivity versus wavelength (nm, bottom axes) and wavenumbers (cm^{-1}, top axis).

Fe^{III}, d^5 metal center has been previously established[47−49] and is here confirmed *via* TD-DFT analysis (Figures S7−S12 and Tables S6−S11). The λ_{max}(LMCT) increases with the degree of conjugation in alkynyls (Np > Ph > $SiMe_3$) within each series (see Table 3), consistent with a transition from the highest-occupied $\pi(C_2R)$ orbital. The energy of the LMCT band is also remarkably reduced by the introduction of the α-diimines (Table 3). Specifically, the LMCT bands in **1a−1c** are red-shifted by ≥0.33 eV from their counterparts in **2a−2c**. This is consistent with the electrochemical data, which indicates that the α-diimines should lower the energy of the

https://doi.org/10.1021/acs.inorgchem.2c01743
Inorg. Chem. 2022, 61, 13442−13452

Table 3. LMCT Characteristics of 1 and 2 in Acetonitrile

	1a	2a	1b	2b	1c	2c
λ_{max} (nm)	681	567	783	648	553	470
ν (cm^{-1})	14 684	17 637	12 771	15 432	18 083	21 277
ε (M^{-1} cm^{-1})	5300	3400	6000	2600	5600	4300
$\Delta\nu$ (2-1)[a]	2953 cm^{-1} (0.37 eV)		2661 cm^{-1} (0.33 eV)		3194 cm^{-1} (0.39 eV)	

[a]$\Delta\nu$ refers to the difference in energy between the maxima of each 1/2 pair.

Scheme 2. Qualitative Illustration of the Frontier Molecular Orbital Interactions in 1′ (Center) from the Interaction of the Tetraimine (Left) with the Molecular Orbitals of σ-Donor Supported Bis-alkynyls 2′ (right) under D_{2h}[a]

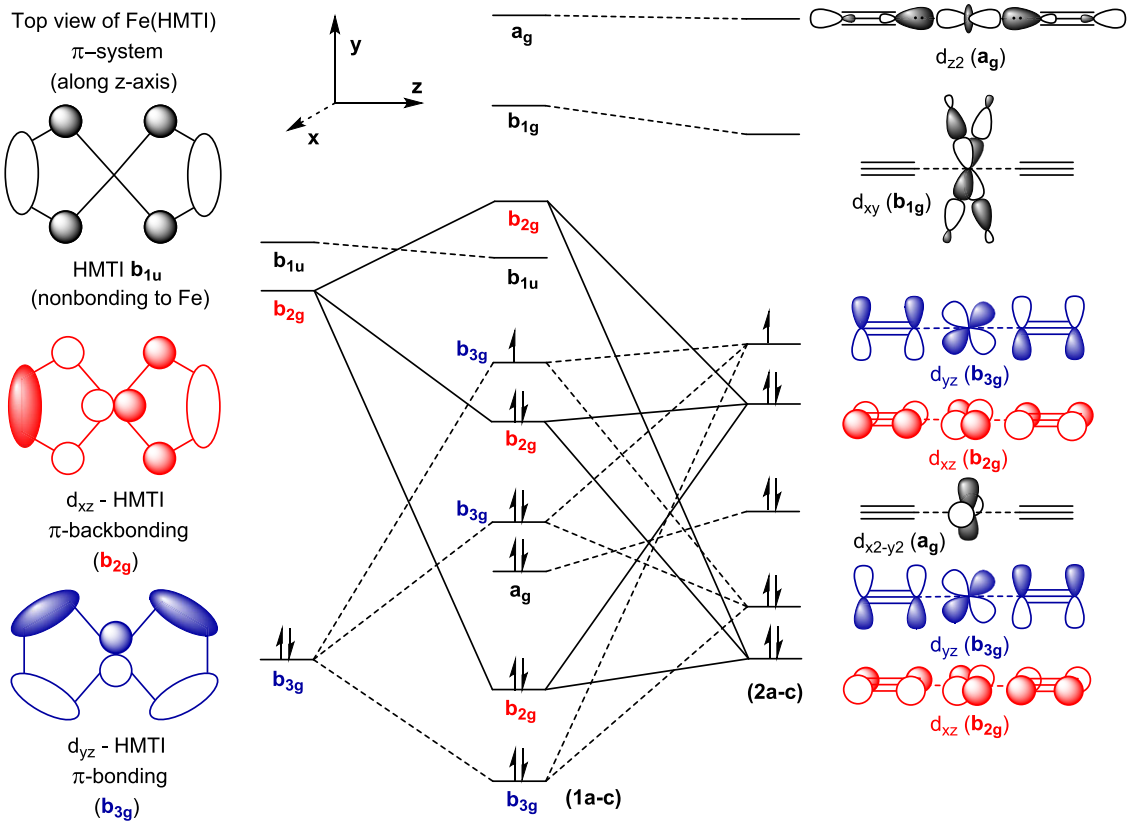

[a]Orbitals shown/labeled in black (a_g, b_{1u}, and b_{1g}) are formally nonbonding with regard to metal dπ orbitals, while those in blue correspond to b_{3g} orbitals and those in red to b_{2g} orbitals.

Fe dπ orbitals, thus reducing E(LMCT). TD-DFT reproduces the experimentally observed order of E(LMCT), although the absolute energy is somewhat underestimated in each case.

Computational Analysis. To better understand the contrasting physical properties between series **1** and **2**, spin-polarized (unrestricted) DFT and TD-DFT calculations on the $[Fe(HMTI/HMC)(C_2R)_2]^+$ moieties were performed using the Gaussian16 suite.[59] The geometries of model complexes **1a′**, **1c′**, and **2a′**−**2c′** were optimized from X-ray structures. The input geometry for **1b′** was created by removing the appropriate eight hydrogen atoms from the structure of **2b**, and the optimized structure for **1b′** exhibits Fe-N, N=C, and C-C_{imine} bond lengths in agreement with those of **1a′** and **1c′** (see Table S5). As noted above, the room temperature magnetic moments for all complexes are too high to be pure low-spin Fe^{III}. Nevertheless, the magnetic moments are consistent with a general dominance of the low-spin state at room temperature (Table S1); therefore, a doublet spin state was used for **1a′**−**1c′** and **2a′**−**2c′**.

Based on the DFT results, a generalized comparison of orbital interactions around the Fe center with the HMC and HMTI ligands is presented in Scheme 2, with an effective symmetry of D_{2h} for both cases. The right side of the scheme illustrates the Fe valence orbitals in series **2**, which consists of (1) four π-orbitals (Fe-$(C_2R)_2$) from the bonding and antibonding combinations between dπ(xz,yz) and π(C≡C) (with the highest b_{3g} half-filled), (2) the nonbonding d_{x2-y2} (a_g), and (3) the empty high-lying dσ (z^2 and xy). The exchange of d_{xy} for the more conventional d_{x2-y2} label as the σ/σ* orbitals results from the choice of coordinates, enabling π-type overlap under D_{2h} symmetry. The left side of Scheme 2 features the three relevant π-type orbitals originating from the two α-diimine units in HMTI. The lower two are of b_{3g} and b_{2g} symmetry and capable of interacting with Fe d_{yz} and d_{xz}, respectively, while the highest of the three, b_{1u}, is nonbonding to Fe dπ due to symmetry mismatching. The combination of the Fe valence orbitals from the right side with the π(α-diimine) from the left side results in the valence MOs for series **1**, where the relative energetic order is consistent with the DFT

https://doi.org/10.1021/acs.inorgchem.2c01743
Inorg. Chem. 2022, 61, 13442−13452

analysis. The main impact is the stabilization of the filled Fe orbitals through the mixing of the d_{xz} with the empty b_{2g}(HMTI). The Fe d_{yz} remains the SOMO in **1** and is slightly stabilized compared to the Fe d_{yz} in **2** in spite of the antibonding interaction with the occupied b_{3g}(HMTI). The slight stabilization of d_{yz}, though counter-intuitive, is due to the strong electron-withdrawing effect of HMTI, which is best illustrated by the *ca.* −0.27 eV shift of the nonbonding d_{x2-y2} orbital from series **2** to series **1**. Finally, the ring contraction from HMC to HMTI also results in increased σ-donation from the nitrogen centers, which raises the energy of the empty d_{xy} by *ca.* 0.24 eV. It must be noted that the relative ordering of the Fe $d\pi(xz,yz)$ orbitals depends on the conjugation of the alkynyl substituent and is thus not rigorously enforced for **1c′** and **2c′**, where the two orthogonal π(C≡C) orbitals are formally degenerate.

Spectroelectrochemical Analysis of 1a and 2a. The changes in the electronic structures of **1a** and **2a** upon reduction or oxidation were probed using UV−Vis and IR spectroelectrochemistry (SEC). Analysis of **1a** was conducted in THF, while SEC of **2a** was conducted in DCM due to solubility constraints. The oxidation states of the bis-alkynyl species will be explicitly denoted by a superscripted charge (*e.g.*, +1 for the initial species, +2 for the one-electron oxidized product and 0 for the one-electron reduced product).

Oxidation of $[\mathbf{2a}]^{+1}$ to $[\mathbf{2a}]^{+2}$ (couple **A** in Figure 2) is accompanied by a decrease in the intensity of the LMCT band and a bathochromic shift of λ_{max} from 587 to 620 nm (Figure S13). A shift in ν(C≡C) from 2070 to 1976 cm^{-1} (Figure S15) is observed in the IR SEC, suggesting a weakening of the alkynyl C≡C bonds due to enhanced π-donation to the electropositive metal center. These changes are consistent with the previous $Fe^{IV/III}$ assignment and are supported by DFT analysis.

Although the reduction of $[\mathbf{2a}]^{+1}$ to $[\mathbf{2a}]^{0}$ (couple **C** in Figure 2) appears reversible in CV, $[\mathbf{2a}]^{0}$ was found to be unstable on the SEC time scale (20−30 minutes). Thus, the spectroscopic features associated with $[\mathbf{2a}]^{0}$ reach a maximum before reduction is complete (gray trace, Figure 4). Nevertheless, the peak profile for $[\mathbf{2a}]^{0}$ can be extracted as the partial decomposition does not introduce interfering spectral features (Figure S17). It is clear from Figure 4 that an intense band at 455 nm emerges upon reduction, while the LMCT band of $[\mathbf{2a}]^{+1}$ at 587 nm is completely bleached. The new band is clearly metal-to-ligand charge transfer (MLCT) in nature, as the feature is reproduced in the TD-DFT analysis of $[\mathbf{2a}]^{0}$, with dominant transitions being HOMO−LUMO at 486.07 nm and HOMO-1−LUMO at 477.77 nm. The HOMO and HOMO-1 are calculated to be 80.4% d_{yz} and 74.2% d_{xz}, respectively, and the LUMO is a π^* orbital of the C_2Ph. Previously, MLCT bands around 370 nm were observed for $Fe^{II}(P\text{-}P)_2(C_2Ph)_2$-type compounds.[60] The lower MLCT energy in $[\mathbf{2a}]^{0}$ reflects insufficient stabilization of $d\pi$ orbitals by HMC, a hard base ligand, compared to softer phosphines. The increase in the $d\pi$ electrons (5 to 6) in $[\mathbf{2a}]^{0}$ results in a significant shift of ν(C≡C) from 2070 cm^{-1} in $[\mathbf{2a}]^{+1}$ to 2009 cm^{-1} (see Figure S18), which indicates substantial $d\pi-\pi^*$(C≡C) backdonation. This is an interesting finding as the predominant M-alkynyl π interaction has been attributed to $d\pi-\pi$(C≡C), filled−filled type, while backdonation was considered negligible.[61] An alternative explanation is that the destabilized metal orbitals result in poorer metal-ligand energy matching, giving rise to higher C anionic character, which would also weaken the C≡C bond.[61] This latter view is better supported both by trends in the ν(C≡C) of **1a−1c** versus **2a−2c** (see the SI) and by DFT analysis and is further elaborated below.

The Vis−NIR SEC for the reduction of $[\mathbf{1a}]^{+1}$ is shown in Figure 5, where two unique, intense transitions at 336 and 762 nm grow in as the structured LMCT band of $[\mathbf{1a}]^{+1}$ is bleached. The low energy (762 nm) band is readily assigned as an MLCT to the tetraimine moiety based on Fe^{II}(HMTI) precedents,[62] which is corroborated by TD-DFT analysis that predicts a pair of Fe-to-HMTI transitions at 588.95 and 632.06 nm giving rise to a single MLCT band (Table S14). The band at 336 nm is attributed to an Fe to C_2Ph MLCT band on the basis of comparison to $[\mathbf{2a}]^{0}$, and it is hypsochromically shifted by 0.97 eV. The TD-DFT analysis agrees with this assignment with the calculated CT transition at 373.16 nm (Table S14). Since the energy of $\pi^*(C_2Ph)$ is relatively constant, the drastic shift of the second MLCT is clearly the result of the stabilization of Fe $d\pi$ in $[\mathbf{1a}]^{0}$ versus $[\mathbf{2a}]^{0}$. The stabilization of Fe $d\pi$ in $[\mathbf{1a}]^{0}$ is also reflected in a small shift of the ν(C≡C): 2082 cm^{-1} in $[\mathbf{1a}]^{+1}$ versus 2075 cm^{-1} in $[\mathbf{1a}]^{0}$ (Figure

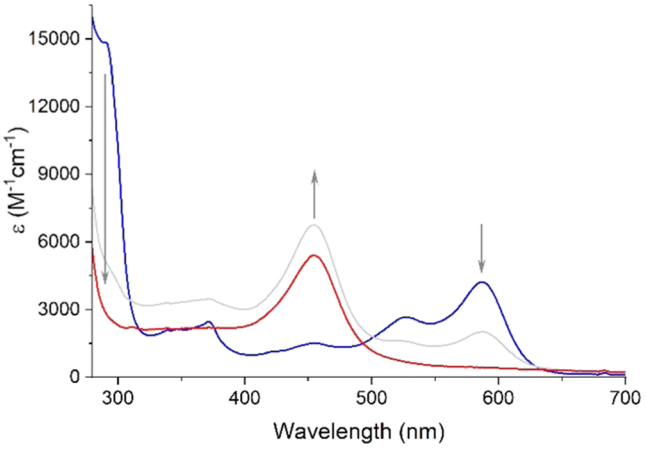

Figure 4. UV−Vis SEC of $[\mathbf{2a}]^{+1}$ (blue, 5 mM) upon reduction to $[\mathbf{2a}]^{0}$ (red) in DCM (0.1 M NBu_4PF_6).

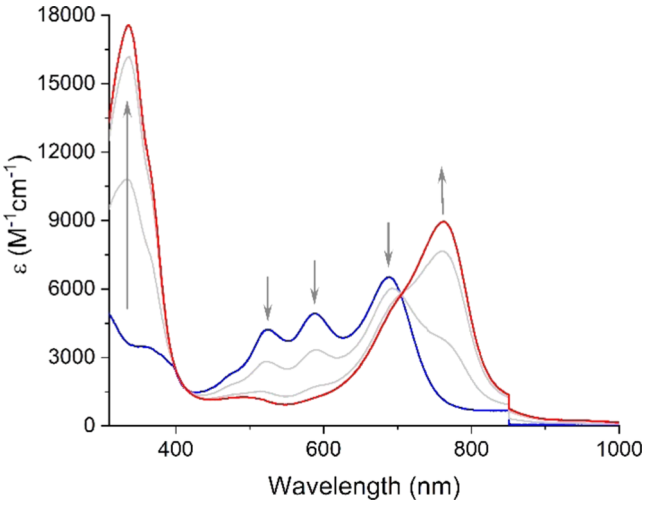

Figure 5. UV−Vis−NIR SEC of $[\mathbf{1a}]^{+1}$ (blue, 5 mM) upon reduction to $[\mathbf{1a}]^{0}$ (red) in THF (0.1 M NBu_4PF_6).

https://doi.org/10.1021/acs.inorgchem.2c01743
Inorg. Chem. 2022, 61, 13442−13452

Scheme 3. Diagram of the Relative Computed Energies of Related Orbitals for $[\mathbf{1a}']^z$ (z = +1, 0, −1) and $[\mathbf{2a}']^z$ (z = +1, 0)[a]

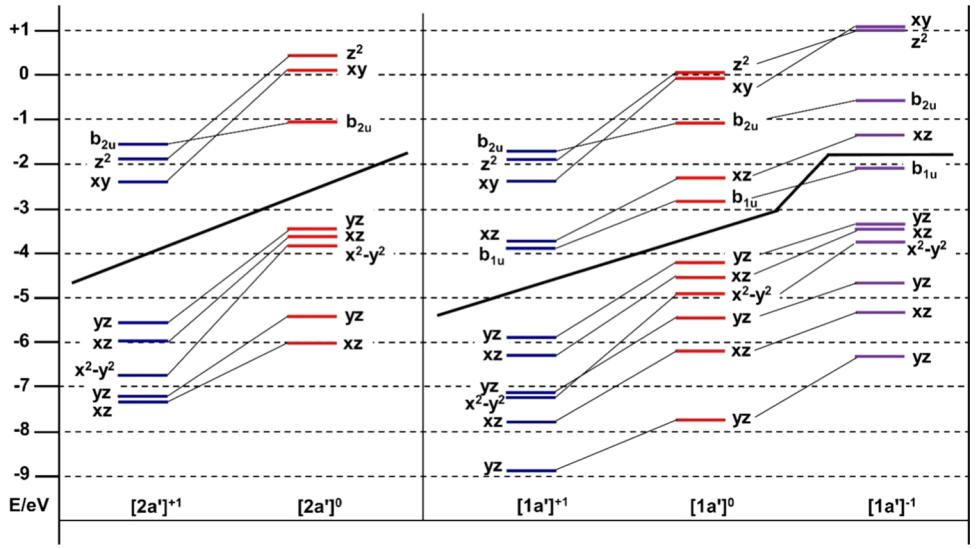

[a]For doublet (z = +1, −1) systems, the α orbital energies are used.

S22). Distinct from the behavior of **2a**, the spectrum of $[\mathbf{1a}]^{+1}$ is fully recovered upon oxidation of $[\mathbf{1a}]^0$ (Figure S23), indicating the robustness of the latter.

Further reduction of $[\mathbf{1a}]^0$ to $[\mathbf{1a}]^{-1}$ (couple **D** in Figure 2), presumably localized at the HMTI ring, was also probed *via* SEC. While the irreversibility of couple **D** prevents meaningful quantification of spectral data, there are some clear and noteworthy changes: the MLCT band at 762 nm in $[\mathbf{1a}]^0$ being shifted to 624 nm, the MLCT band at 336 nm being replaced by a pair of new bands at 428 and 369 nm (Figure S25), and the ν(C≡C) at 2075 cm^{-1} being shifted to 2024 cm^{-1} (Figure S27). These features are consistent with the significantly reduced π-accepting character of the HMTI ring upon the second reduction (**D**).

To further analyze the SEC results, a comparison of the calculated orbital energies for optimized models $[\mathbf{1a}']^z$ and $[\mathbf{2a}']^z$ is depicted in Scheme 3. Orbitals with metal characters are denoted by the d-orbital labels under D_{2h}. Orbitals of entirely ligand character are denoted by their appropriate symmetry labels (b_{2u} refers to the lowest-energy π^* combination of the phenylacetylide ligands; b_{1u} refers to the lowest-energy π^* of the tetraimine ring). A heavy solid line denotes the boundary between the occupied/partially occupied and the unoccupied orbitals. It was assumed that both $[\mathbf{1a}']^0$ and $[\mathbf{2a}']^0$ are low-spin (diamagnetic) since the ferrous complexes Fe(HMC)$(CN)_2$ and Fe(HMTI)$(CN)_2$ are both low-spin.[63,64]

Reduction of $[\mathbf{2a}']^{+1}$ results in a substantial increase in the energy of all metal-centered orbitals, ranging from +1.34 to +2.90 eV, with the magnitude of the increase correlating with the degree of metal character in the orbital of $[\mathbf{2a}']^0$. This is consistent with a true metal-centered reduction. Furthermore, Fe contributes 74.2 and 80.4% in the HOMO (d_{yz}) and HOMO-1 (d_{xz}) of $[\mathbf{2a}']^0$, respectively, reflecting an energetic mismatch between the Fe^{II} dπ and filled alkynyl π-orbitals in $[\mathbf{2a}']^0$.

The changes upon reducing $[\mathbf{1a}']^{+1}$ to $[\mathbf{1a}']^0$ are comparatively less dramatic. The HOMO of $[\mathbf{1a}']^0$ lies 1.57 eV above the SOMO (α) of $[\mathbf{1a}']^{+1}$, while the same shift is 2.14 eV for **2a′**. Concurrently, the Fe contributions to the frontier orbitals in $[\mathbf{1a}']^0$, 61.2% (HOMO d_{yz}) and 50.1% (HOMO-1 d_{xz}), are significantly lower than those in $[\mathbf{2a}']^0$, with the remaining density lying on the C_2Ph and α-diimine moieties. Interestingly, the iron-alkynyl σ-bond is also affected: the total Fe (s + d) character of the Fe-C σ^* is 94.6% in $[\mathbf{2a}']^0$ (LUMO + 5) but only 75.8% in $[\mathbf{1a}']^0$ (LUMO + 7). Thus, the π acceptor nature of HMTI helps to disperse the electron density localized on the Fe center and hence diminish the energetic cost of reduction.

The changes in the composition of frontier orbitals also help to explain the shifts of ν(C≡C) upon reduction. As mentioned above, the weakening of the C≡C bond could reflect either increased backdonation into the C_2Ph π^* and/or an enlarged energy gap between the filled Fe and C_2Ph orbitals. The latter would impart a higher ionic character to the Fe-C bond, which would weaken the C≡C bond by virtue of the C-C σ-antibonding nature of the alkynyl anion. In the case of **2a**, a −61 cm^{-1} (calc. −76.79 cm^{-1}) shift is observed upon the first reduction—consistent with Fe dπ to $\pi(C_2Ph)$ backbonding, increased ionic Fe-C bond character, or both—as the energies of the metal-centered orbitals increase. In contrast, the same shift in **1a** is merely −7 cm^{-1} (calc. −0.70 cm^{-1}), reflecting delocalization of the added electron. The decreased π accepting capacity of the α-diimines in $[\mathbf{1a}]^{-1}$ restores the Fe dπ-$\pi(C_2)$ energetic mismatch, and thus a more dramatic shift in ν(C≡C) of −51 cm^{-1} versus $[\mathbf{1a}]^0$ (calc. −28.33 cm^{-1}). The growth of metal character in the dπ/dσ−C_2R antibonding orbitals suggests a more ionic Fe-C bond as the energy of the metal-centered orbitals is increased with reduction: an effect that is mitigated by the electron-withdrawing nature of HMTI.

Further Discussion. As noted in the Introduction, previous work on iron-alkynyl complexes has largely been based on complexes supported by "soft" supporting ligand frameworks (L), which preferentially stabilize the Fe^{II} state (Chart 1, **I** and **II**), though some work has been performed on Fe^{III} complexes of the hard base cyclam (Chart 1, **III**). Here, the use of (spectro)electrochemistry affords a rare opportunity to compare Fe^{III} alkynyls with different types of supporting macrocyles across oxidation states. In particular, Fe^{II} complexes

https://doi.org/10.1021/acs.inorgchem.2c01743
Inorg. Chem. 2022, 61, 13442−13452

$[\mathbf{1a}]^0$ and $[\mathbf{2a}]^0$ are comparable to $Fe^{II}(dmpe)_2(C_2Ph)_2$ and $Fe^{II}(depe)_2(C_2Ph)_2$ (depe=1,2-bis(diethylphosphino)ethane). As noted above, $[\mathbf{2a}]^0$ exhibits a much lower energy Fe^{II} to C_2Ph MLCT band (455 nm) than $Fe^{II}(dmpe)_2(C_2Ph)_2$ (364 nm) and $Fe^{II}(depe)_2(C_2Ph)_2$ (375 nm),[60] implying that the Fe-centered molecular orbitals lie higher in energy for the former. Likewise, the $\nu(C{\equiv}C)$ of $[\mathbf{2a}]^0$ (2009 cm^{-1}) is lower in energy than those of $Fe^{II}(dmpe/depe)_2(C_2Ph)_2$ (2035−2037 cm^{-1}).[60] In contrast, $[\mathbf{1a}]^0$ exhibits higher energy Fe^{II} to C_2Ph (336 nm) and $\nu(C{\equiv}C)$ (2075 cm^{-1}) bands, suggesting a slightly lower energy set of Fe^{II} $d\pi$ orbitals than those of the phosphine-supported species. However, the relative C_2Ph to Fe^{III} LMCT energies of $[\mathbf{1a}]^{+1}$ versus $Fe(dmpe)_2(C_2Ph)_2^+$ (820 nm in dichloromethane)[31] suggest that the SOMO of the latter is slightly lower in energy. This seemingly contradictory result can be rationalized by considering the dual nature of HMTI as both π-donor and π-acceptor: in the more electron-rich Fe^{II} state, the π-acceptor nature is dominant, whereas the donor properties of HMTI become more competitive in the Fe^{III} oxidation state as backbonding is diminished. The phosphine-based ligands of $Fe(dmpe)_2(C_2Ph)_2^+$ lack π-donor character, and so the frontier Fe^{III} $d\pi$ only experiences the net stabilization due to weak backbonding.

CONCLUSIONS

Availability of novel tetraimine complexes **1a−1c** and their tetraamine counterparts **2a−2c** allows for a close inspection of the impact of ring unsaturation on the electronic structures through X-ray diffraction, voltammetry, spectroelectrochemistry, and DFT analysis. All evidences point to the depression of the formally Fe-centered occupied orbitals and the concomitant reduction of the gap between these and the π-donating orbitals of the axial alkynyl ligands. The overall result appears to be a more balanced (covalent) Fe-alkynyl π-bonding, which implies greater conjugation across the RC_2-Fe-C_2R π orbital system. Work is underway to examine both the photophysical properties of the LMCT/MLCT states in these compounds and possible new reactivity owing to the enhanced Fe-C covalency.

EXPERIMENTAL SECTION

General Information. The isomers of HMC (5,5,7,12,12,14-hexamethyl-1,4,8,11-tetraazacyclotetradecane) were prepared, and *meso*-HMC was isolated according to literature procedures.[65] Trimethylsilylacetylene (HC_2TMS) and phenylacetylene (HC_2Ph) were purchased from Oakwood Chemical, and 1-(trimethylsilylethynyl)naphthalene ($TMSC_2Np$) was also prepared according to the literature procedure.[66] Dry acetonitrile was purchased from Acros Organics and stored under an inert atmosphere. Dry THF was distilled over Na/benzophenone under a nitrogen atmosphere. All air-sensitive reactions were performed under an N_2 atmosphere using standard Schlenk line techniques.

Spectroscopic Measurements. ESI-MS was performed with an Advion Mass Spectrometer. A JASCO FT-IR 6300 was used for all infrared spectra (solid-state data collected *via* ATR on ZnSe—see the SI). For general UV−Vis spectra, a JASCO V-670 UV−Vis−NIR spectrophotometer was used. Magnetic moments for **1a−1c** and **2a−2c** were determined using the Evans Method[51] with a ferrocene internal standard and insert on a Varian INOVA300 NMR. The solid-state magnetic moment of $Fe(HMC)(SO_4)(HSO_4)$ (which is sparingly soluble in common organic solvents) was determined on a Johnson-Matthey magnetic susceptibility balance. Electrochemical measurements were obtained using a CHI620A voltammetric analyzer using a glassy carbon working electrode, a platinum counter electrode, and an Ag/AgCl pseudo-reference electrode. Elemental analyses were conducted by Atlantic Microlab, Inc. (Norcross, Georgia). Spectroelectrochemical data were collected in an OTTLE (optically transparent thin-layer electrochemistry)[67] liquid-sample cell with a CaF_2 window (*ca.* 0.2 mm path length), Pt mesh working and auxiliary electrodes, and an Ag pseudo-reference electrode on a JASCO V-780 UV−Vis−NIR spectrophotometer and a JASCO FT-IR 6300.

Computational Methods. All computations were performed using Gaussian16[59] with the MN12-L functional,[68] Def2-TZVP basis set for Fe and Si and Def2-SVP for all other atoms.[69] Solvent effects were included for all calculations using a polarizable continuum model (CPCM)[70] with the appropriate solvent. Frequency checks produced no negative frequencies, indicating that the structures were indeed at a minimum. The major atomic contributions to molecular orbitals of interest on the optimized structures were assessed as needed using the Pop=Orbitals=n keywords. Additional details, including input and optimized coordinates, are given in the SI.

The functionals MN15[71] and B3LYP[72] (with dispersion)[73] were also tested. MN15 performed comparably to MN12-L for geometry optimizations but dramatically overestimated the energy of the LMCT band. B3LYP performed just as well as MN12-L on excitation energies, but convergence of the geometries proved more difficult and resource intensive. MN12-L was therefore used to achieve reasonable results at an acceptable computational cost.

Syntheses. The syntheses for $Fe(HMC)(SO_4)(HSO_4)$, **1a**, and **2a** are given below as representative synthetic methods. The syntheses for **1/2b** and **1/2c** are given in the Supporting Information. For **1a−1c**, the lithium acetylide (LiC_2R) was uniformly prepared using a high excess of *n*-BuLi, as this later serves as the source of strong base for the oxidative dehydrogenation of HMC to HMTI (see Synthesis section of Results and Discussion).

Synthesis of Fe(meso-HMC)(HSO$_4$)(SO$_4$). Briefly, 1.00 g (3.52 mmol) of *meso*-HMC was dissolved in 120 mL of methanol. The resulting solution was purged with nitrogen prior to the addition of 1.2 equiv of $Fe(SO_4)_2{\cdot}7H_2O$ (1.56 g, 4.17 mmol). The resulting mixture was heated for 2.5 h to approximately 50 °C while the N_2 atmosphere was maintained. Oxygen was then bubbled through the solution for 15 min prior to the addition of 4 mL H_2SO_4 (95 w/w%, excess), resulting in the formation of a deep orange solution. Oxygen was vigorously bubbled through the solution over the next 2.75 h, during which time a pale green precipitate formed. The mixture was filtered, and the recovered solid was washed with acetone and diethyl ether to yield 1.00 g of the desired complex (1.87 mmol, 53% based on HMC). ESI-MS(m/z): $[Fe(HMC)(HSO_4)_2]^+$, 534.4, $[Fe(HMC)(SO_4)_2]^-$, 532.3; Elem. Anal. Found (calcd.) for $FeN_4C_{16}H_{38.5}S_2O_{8.75}$ ($Fe(HMC)(SO_4)(HSO_4){\cdot}0.75H_2O$): C 35.35 (35.13); H 7.03 (7.09); N 10.11 (10.24). IR (cm^{-1}): N-H: 3125 (m), O-H: 3165 (m). μ_{eff} = 5.91 BM.

*Synthesis of [Fe(meso-HMTI)(C$_2$Ph)$_2$]BPh$_4$ (**1a**).* $Fe(HMC)(SO_4)(HSO_4)$ (0.101 g, 0.190 mmol) was dissolved in 7 mL of dry THF and cooled to −78 °C, to which was added LiC_2Ph (0.73 mmol, prepared from HC_2Ph and excess *n*-BuLi in 6 mL THF). The resulting solution was held at −78 °C for 30 min, then transferred to an ice bath for an additional 1 h. Oxygen was bubbled through the deep green solution for less than 2 min with the simultaneous addition of a few drops of methanol. Sodium tetraphenylborate (221 mg, 0.65 mmol) was then added, and the solution was filtered through Celite, which was rinsed with DCM until the filtrate ran clear. Excess hexanes and diethyl ether were added to the filtrate to precipitate the crude solid. Final purification was accomplished over silica (eluting with DCM), followed by recrystallization from DCM/hexanes to yield 42.2 mg of the indigo product (0.049 mmol, 26% based on $Fe(HMC)(SO_4)(HSO_4)$). ESI-MS (m/z): $[M]^+$, 534.7. Elem. Anal. Found (calcd.) for $FeN_4C_{56.15}H_{58.3}BCl_{0.3}$ (**1a**·$0.15CH_2Cl_2$): C 77.94 (77.83); H 6.91 (6.78); N 6.64 (6.47). Visible spectrum, λ_{max} (nm, ε (M^{-1} cm^{-1})): 681 (5300), 585 (4600), 525 (3800). IR (cm^{-1}): C≡C: 2082 (w), C═N: 1536 (w), C═C_{Ph}: 1593 (w). Cyclic voltammetry [$E_{1/2}$/V, ΔE_p/V (vs Fc/Fc^+), $i_{p,c}/i_{p,a}$]: $Fe^{III/II}$, −0.523, 0.058, 1.02. μ_{eff} = 3.0 BM.

https://doi.org/10.1021/acs.inorgchem.2c01743
Inorg. Chem. 2022, 61, 13442−13452

*Synthesis of [Fe(meso-HMC)(C_2Ph)$_2$]BPh$_4$ (**2a**).* Dry Fe(HMC)-(SO_4)(HSO_4) (0.100 g, 0.187 mmol) was suspended in THF (5 mL) and cooled in a dry ice/acetone bath. A solution of LiC_2Ph (0.08 mL, 0.7 mmol; in 5 mL THF) was transferred to a flask with Fe(HMC)(SO_4)(HSO_4) under nitrogen. The resulting mixture was held at −78 °C for 1.25 h before warming to room temperature for over 50 min. Subsequently, the solution was transferred to a flask containing 204 mg (0.6 mmol) $NaBPh_4$ under nitrogen. The resultant blue-green solution was exposed to air and immediately filtered through silica, eluting the pink product with DCM. The crude solid was precipitated with hexanes and isolated by filtration prior to washing with diethyl ether and hexanes. Purification over silica with 6:1 DCM:hexanes yielded the pure product, which was obtained as 53.2 mg of maroon powder following recrystallization from DCM/hexanes (0.062 mmol, 33% yield based on Fe(HMC)(SO_4)(HSO_4)). ESI-MS (m/z): $[M]^+$, 542.0. Elem. Anal. Found (calcd.) for $FeN_4C_{56.75}H_{67.5}BCl_{1.5}$ (**2a**·0.75CH_2Cl_2): C 74.07 (73.65); H 7.48 (7.35); N 6.17 (6.05). Visible spectrum, λ_{max} (nm, ε (M^{-1} cm^{-1})): 567 (3400), 512 (2400), 453 (1600), 368 (2700). IR (cm^{-1}): N-H: 3220 (m), C≡C: 2070 (w), C=C_{Ph}: 1592 (m). Cyclic voltammetry [$E_{1/2}$/V, ΔE_p/V (vs Fc/Fc^+), $i_{p,c}/i_{p,a}$]: $Fe^{III/II}$, −1.150, 0.070, 1.04. μ_{eff} = 3.6 BM.

■ ASSOCIATED CONTENT

Supporting Information

The Supporting Information is available free of charge at https://pubs.acs.org/doi/10.1021/acs.inorgchem.2c01743.

Additional experimental, crystallographic, and computational details, including IR spectra, time-dependent DFT (TD-DFT) spectral assignments, additional spectroelectrochemical spectra, *etc.* (PDF)

Accession Codes

CCDC 2173367−2173373 contain the supplementary crystallographic data for this paper. These data can be obtained free of charge via www.ccdc.cam.ac.uk/data_request/cif, or by emailing data_request@ccdc.cam.ac.uk, or by contacting The Cambridge Crystallographic Data Centre, 12 Union Road, Cambridge CB2 1EZ, U.K.; fax: +44 1223 336033.

■ AUTHOR INFORMATION

Corresponding Author

Tong Ren − *Department of Chemistry, Purdue University, West Lafayette, Indiana 47907, United States;* orcid.org/0000-0002-1148-0746; Email: tren@purdue.edu

Authors

Reese A. Clendening − *Department of Chemistry, Purdue University, West Lafayette, Indiana 47907, United States*

Matthias Zeller − *Department of Chemistry, Purdue University, West Lafayette, Indiana 47907, United States;* orcid.org/0000-0002-3305-852X

Complete contact information is available at: https://pubs.acs.org/10.1021/acs.inorgchem.2c01743

Notes

The authors declare no competing financial interest.

■ ACKNOWLEDGMENTS

The authors thank the National Science Foundation for generously supporting this work (CHE 2102049). R.A.C. thanks Mr. Xi Wang for synthetic assistance with **2c**, and Dr. Ashley Schuman for providing $TMSC_2Np$. The authors gratefully acknowledge Mr. Prakhar Gautam for cover design assistance.

■ REFERENCES

(1) Long, N. J.; Williams, C. K. Metal Alkynyl Complexes: Synthesis and Materials. *Angew. Chem., Int. Ed.* **2003**, *42*, 2586−2617.

(2) Haque, A.; Al-Balushi, R. A.; Al-Busaidi, I. J.; Muhammad, S. Khan.; Raithby, P. R. Rise of Conjugated Poly-ynes and Poly(Metallaynes): From Design Through Synthesis to Structure−Property Relationships and Applications. *Chem. Rev.* **2018**, *118*, 8474−8597.

(3) Bryce, M. R. A review of functional linear carbon chains (oligoynes, polyynes, cumulenes) and their applications as molecular wires in molecular electronics and optoelectronics. *J. Mater. Chem. C* **2021**, *9*, 10524.

(4) Paul, F.; Lapinte, C. Organometallic Molecular Wires and Other Nanoscale-sized Devices. An Approach using the Organoiron (dppe)Cp*Fe Building Block. *Coord. Chem. Rev.* **1998**, *178−180*, 431−509.

(5) Launay, J. P. Mixed-Valent Compounds and their Properties - Recent Developments. *Eur. J. Inorg. Chem.* **2020**, *2020*, 329−341.

(6) Gendron, F.; Groizard, T.; Le Guennic, B.; Halet, J. F. Electronic Properties of Poly-Yne Carbon Chains and Derivatives with Transition Metal End-Groups. *Eur. J. Inorg. Chem.* **2020**, *2020*, 667−681.

(7) Ho, C.-L.; Yu, Z.-Q.; Wong, W.-Y. Multifunctional polymetallaynes: properties, functions and applications. *Chem. Soc. Rev.* **2016**, *45*, 5264−5295.

(8) Xu, L.; Ho, C.-L.; Liu, L.; Wong, W.-Y. Molecular/polymeric metallaynes and related molecules: Solar cell materials and devices. *Coord. Chem. Rev.* **2018**, *373*, 233−257.

(9) Green, K. A.; Cifuentes, M. P.; Samoc, M.; Humphrey, M. G. Metal alkynyl complexes as switchable NLO systems. *Coord. Chem. Rev.* **2011**, *255*, 2530−2541.

(10) Zhou, G.-J.; Wong, W.-Y. Organometallic acetylides of Pt(II), Au(I) and Hg(II) as new generation optical power limiting materials. *Chem. Soc. Rev.* **2011**, *40*, 2541−2566.

(11) Zhu, H.; Pookpanratana, S. J.; Bonevich, J. E.; Natoli, S. N.; Hacker, C. A.; Ren, T.; Suehle, J. S.; Richter, C. A.; Li, Q. Redox-Active Molecular Nanowire Flash Memory for High-Endurance and High-Density Non-Volatile Memory Applications. *ACS Appl. Mater. Interfaces* **2015**, *7*, 27306−27313.

(12) Milan, D. C.; Vezzoli, A.; Planje, I. J.; Low, P. J. Metal bis(acetylide) complex molecular wires: concepts and design strategies. *Dalton Trans.* **2018**, *47*, 14125−14138.

(13) Bruce, M. I. Organometallic Chemistry of Vinylidene and Related Unsaturated Carbenes. *Chem. Rev.* **1991**, *91*, 197−257.

(14) Bruce, M. I. Some complexes of all-carbon ligands and related chemistry. *Coord. Chem. Rev.* **1997**, *166*, 91−119.

(15) Bruce, M. I. Transition Metal Complexes Containing Allenylidene, Cumulenylidene, and Related Ligands. *Chem. Rev.* **1998**, *98*, 2797−2858.

(16) Szafert, S.; Gladysz, J. A. Carbon in One Dimension: Structural Analysis of the Higher Conjugated Polyynes. *Chem. Rev.* **2003**, *103*, 4175−4206.

(17) Szafert, S.; Gladysz, J. A. Update 1 of: Carbon in One Dimension: Structural Analysis of the Higher Conjugated Polyynes. *Chem. Rev.* **2006**, *106*, 1−33.

(18) Costuas, K.; Rigaut, S. Polynuclear carbon-rich organometallic complexes: clarification of the role of the bridging ligand in the redox properties. *Dalton Trans.* **2011**, *40*, 5643−5658.

(19) Nast, R. Coordination Chemistry of Metal Alkynyl Compounds. *Coord. Chem. Rev.* **1982**, *47*, 89−124.

(20) Hall, M. R.; Moggach, S. A.; Low, P. J. Syntheses and Structures of trans-bis(Alkenylacetylide) Ruthenium Complexes. *Chem. Asian J.* **2021**, *16*, 3385−3403.

(21) Miller-Clark, L. A.; Ren, T. Syntheses and material applications of Ru(II)(bisphosphine)2 alkynyls. *J. Organomet. Chem.* **2021**, *951*, No. 122003.

(22) Bruce, M. I.; Low, P. J.; Costuas, K.; Halet, J.-F.; Best, S. P.; Heath, G. A. Oxidation Chemistry of Metal-Bonded C4 Chains: A Combined Chemical, Spectroelectrochemical, and Computational Study. *J. Am. Chem. Soc.* **2000**, *122*, 1949−1962.

(23) Bruce, M. I.; Ellis, B. G.; Low, P. J.; Skelton, B. W.; White, A. H. Syntheses, structures, and spectro-electrochemistry of {Cp*(PP)Ru} C CC C{Ru(PP)Cp*} (PP = dppm, dppe) and their mono- and dicationst. *Organometallics* **2003**, *22*, 3184−3198.
(24) Zhu, Y.; Clot, O.; Wolf, M. O.; Yap, G. P. A. Effect of Ancillary Ligands on Ru(II) on Electronic Delocalization in Ruthenium(II) Bisferrocenylacetylide Complexes. *J. Am. Chem. Soc.* **1998**, *120*, 1812−1821.
(25) Tanaka, Y.; Kato, Y.; Tada, T.; Fujii, S.; Kiguchi, M.; Akita, M. "Doping" of Polyyne with an Organometallic Fragment Leads to Highly Conductive Metallapolyyne Molecular Wire. *J. Am. Chem. Soc.* **2018**, *140*, 10080−10084.
(26) Meng, F. B.; Hervault, Y. M.; Norel, L.; Costuas, K.; Van Dyck, C.; Geskin, V.; Cornil, J.; Hng, H. H.; Rigaut, S.; Chen, X. D. Photo-modulable molecular transport junctions based on organometallic molecular wires. *Chem. Sci.* **2012**, *3*, 3113−3118.
(27) Meng, F. B.; Hervault, Y. M.; Shao, Q.; Hu, B. H.; Norel, L.; Rigaut, S.; Chen, X. D. Orthogonally modulated molecular transport junctions for resettable electronic logic gates. *Nat. Commun.* **2014**, *5*, No. 3023.
(28) Tanaka, Y.; Kato, Y.; Sugimoto, K.; Kawano, R.; Tada, T.; Fujii, S.; Kiguchi, M.; Akita, M. Single-molecule junctions of multinuclear organometallic wires: long-range carrier transport brought about by metal-metal interaction. *Chem. Sci.* **2021**, *12*, 4338−4344.
(29) Saha Roy, S.; Sil, A.; Giri, D.; Chowdhury, S. R.; Mishra, S.; Patra, S. K. Diruthenium(ii)-capped oligothienylethynyl bridged highly soluble organometallic wires exhibiting long-range electronic coupling. *Dalton Trans.* **2018**, *47*, 14304−14317.
(30) Roy, S. S.; Chowdhury, S. R.; Mishra, S.; Patra, S. K. Role of Substituents at 3-position of Thienylethynyl Spacer on Electronic Properties in Diruthenium(II) Organometallic Wire-like Complexes. *Chem. Asian J.* **2020**, *15*, 3304−3313.
(31) Wong, C.-Y.; Che, C.-M.; Chan, M. C. W.; Han, J.; Leung, K.-H.; Phillips, D. L.; Wong, K.-Y.; Zhu, N. Probing Ruthenium-Acetylide Bonding Interactions: Synthesis, Electrochemistry, and Spectroscopic Studies of Acetylide-Ruthenium Complexes Supported by Tetradentate Macrocyclic Amine and Diphosphine Ligands. *J. Am. Chem. Soc.* **2005**, *127*, 13997−14007.
(32) Graedel, T. E.; Harper, E. M.; Nassar, N. T.; Nuss, P.; Reck, B. K. Criticality of metals and metalloids. *Proc. Natl. Acad. Sci. U.S.A.* **2015**, *112*, 4257−4262.
(33) Narvor, N. L.; Lapinte, C. First C_4 Bridged Mixed-valence Iron(II)-Iron(III) Complex Delocalized on the Infrared Timescale. *J. Chem. Soc., Chem. Commun.* **1993**, 357−359.
(34) Akita, M.; Chung, M.-C.; Sakurai, A.; Sugimoto, S.; Terada, M.; Tanaka, M.; Moro-oka, Y. Synthesis and Structure Determination of the Linear Conjugated Polyynyl and Polyynediyl Iron Complexes Fp*-(CC)n-X (X = H (n = 1, 2); X = Fp* (n = 1, 2, 4); Fp* = (5-C5Me5)Fe(CO)2). *Organometallics* **1997**, *16*, 4882−4888.
(35) Halet, J.-F.; Lapinte, C. Charge delocalization vs localization in carbon-rich iron mixed-valence complexes: A subtle interplay between the carbon spacer and the (dppe)Cp*Fe organometallic electrophore. *Coord. Chem. Rev.* **2013**, *257*, 1584−1613.
(36) Lissel, F.; Fox, T.; Blacque, O.; Polit, W.; Winter, R. F.; Venkatesan, K.; Berke, H. Stepwise Construction of an Iron-Substituted Rigid-Rod Molecular Wire: Targeting a Tetraferra−Tetracosa−Decayne. *J. Am. Chem. Soc.* **2013**, *135*, 4051−4060.
(37) Lissel, F.; Schwarz, F.; Blacque, O.; Riel, H.; Lortscher, E.; Venkatesan, K.; Berke, H. Organometallic Single-Molecule Electronics: Tuning Electron Transport through X(diphosphine)(2)-FeC4Fe(diphosphine)(2)X Building Blocks by Varying the Fe-X-Au Anchoring Scheme from Coordinative to Covalent. *J. Am. Chem. Soc.* **2014**, *136*, 14560−14569.
(38) Berben, L. A. Toward Acetylide and N-Hetercycle-Bridged Materials with Strong Electronic and Magnetic Coupling. Ph.D. Dissertation, University of California: Berkeley, 2005.
(39) Berben, L. A.; Long, J. R. Synthesis and Alkali Metal Ion-Binding Properties of a Chromium(III) Triacetylide Complex. *J. Am. Chem. Soc.* **2002**, *124*, 11588−11589.
(40) Sun, C.; Thakker, P. U.; Khulordava, L.; Tobben, D. J.; Greenstein, S. M.; Grisenti, D. L.; Kantor, A. G.; Wagenknecht, P. S. Trifluoropropynyl as a Surrogate for the Cyano Ligand and Intense, Room-Temperature, Metal-Centered Emission from Its Rh(III) Complex. *Inorg. Chem.* **2012**, *51*, 10477−10479.
(41) Sun, C.; Turlington, C. R.; Thomas, W. W.; Wade, J. H.; Stout, W. M.; Grisenti, D. L.; Forrest, W. P.; VanDerveer, D. G.; Wagenknecht, P. S. Synthesis of cis and trans Bis-alkynyl Complexes of Cr(III) and Rh(III) Supported by a Tetradentate Macrocyclic Amine: A Spectroscopic Investigation of the M(III)−Alkynyl Interaction. *Inorg. Chem.* **2011**, *50*, 9354−9364.
(42) Hoffert, W. A.; Shores, M. P. Crystallographic coincidence of two bridging species in a dinuclear CoIII ethynylbenzene complex. *Acta Crystallogr., Sect. E: Struct. Rep. Online* **2011**, *67*, m853−m854.
(43) Hoffert, W. A.; Kabir, M. K.; Hill, E. A.; Mueller, S. M.; Shores, M. P. Stepwise acetylide ligand substitution for the assembly of ethynylbenzene-linked Co(III) complexes. *Inorg. Chim. Acta* **2012**, *380*, 174−180.
(44) Banziger, S. D.; Ren, T. Syntheses, Structures and Bonding of 3d Metal Alkynyl Complexes of Cyclam and Its Derivatives. *J. Organomet. Chem.* **2019**, *885*, 39−48.
(45) Ren, T. A Sustainable Metal Alkynyl Chemistry: 3d Metals and Polyaza Macrocyclic Ligands. *Chem. Commun.* **2016**, *52*, 3271−3279.
(46) Cao, Z.; Forrest, W. P.; Gao, Y.; Fanwick, P. E.; Zhang, Y.; Ren, T. New Iron(III) Bis(acetylide) Compounds Based on the Iron Cyclam Motif. *Inorg. Chem.* **2011**, *50*, 7364−7366.
(47) Cao, Z.; Forrest, W. P.; Gao, Y.; Fanwick, P. E.; Ren, T. trans-[Fe(cyclam)(C2R)2]+: A New Family of Iron(III) Bis-Alkynyl Compounds. *Organometallics* **2012**, *31*, 6199−6206.
(48) Cao, Z.; Fanwick, P. E.; Forrest, W. P.; Gao, Y.; Ren, T. New Fe(III)(cyclam) Complexes Bearing Axially Bound geminal-Diethynylethenes. *Organometallics* **2013**, *32*, 4684−4689.
(49) Clendening, R. A.; Ren, T. Mono- and Bis-alkynyl Iron Complexes Supported by a "Softened" Tetraaza Macrocycle. *Eur. J. Inorg. Chem.* **2022**, *2022*, No. e202101021.
(50) Toma, H. E.; Stadler, E. Oxidative dehydrogenation of an iron-tetraazacyclotetradecatriene complex. *Inorg. Chim. Acta* **1986**, *119*, 49−53.
(51) Evans, D. F. The Determination of the Paramagnetic Susceptibility of Substances in Solution by Nuclear Magnetic Resonance. *J. Chem. Soc.* **1959**, 2003−2005.
(52) Judkins, E. C.; Zeller, M.; Ren, T. Synthesis and Characterizations of Macrocyclic Cr(III) and Co(III) 1-Ethynyl Naphthalene and 9-Ethynyl Anthracene Complexes: An Investigation of Structural and Spectroscopic Properties. *Inorg. Chem.* **2018**, *57*, 2249−2259.
(53) Pal, P. K.; Chowdhury, S.; Drew, M. G. B.; Datta, D. The electrooxidation of the tetraphenylborate ion revisited. *New J. Chem* **2002**, *26*, 367−371.
(54) Field, L. D.; George, A. V.; Laschi, F.; Malouf, E. Y.; Zanello, P. Electrochemistry of acetylide Complexes of Iron. *J. Organomet. Chem.* **1992**, *435*, 347−356.
(55) Hess, C. R.; Weyhermuller, T.; Bill, E.; Wieghardt, K. [{Fe(tim)}$_2$]: An Fe-Fe Dimer Containing an Unsupported Metal-Metal Bond and Redox-Active N_4 Macrocyclic Ligands. *Angew. Chem., Int. Ed.* **2009**, *48*, 3703−3706.
(56) Hess, C. R.; Weyhermuller, T.; Bill, E.; Wieghardt, K. Influence of the Redox Active Ligand on the Reactivity and Electronic Structure of a Series of Fe(TIM) Complexes. *Inorg. Chem.* **2010**, *49*, 5686−5700.
(57) Bard, A. J.; Faulkner, L. R. *Electrochemical Methods*, 2nd ed.; John Wiley & Sons: New York, 2001.
(58) Dabrowiak, J. C.; Lovecchio, F. V.; Busch, D. H. Synthesis and electrochemical behavior of a new series of macrocyclic complexes of iron produced by oxidative dehydrogenation and tautomerization. *J. Am. Chem. Soc.* **1972**, *94*, 5502−5504.
(59) Frisch, M. J.; Trucks, G. W.; Schlegel, H. B.; Scuseria, G. E.; Robb, M. A.; Cheeseman, J. R.; Scalmani, G.; Barone, V.; Petersson, G. A.; Nakatsuji, H.; Li, X.; Caricato, M.; Marenich, A. V.; Bloino, J.; Janesko, B. G.; Gomperts, R.; Mennucci, B.; Hratchian, H. P.; Ortiz, J.

https://doi.org/10.1021/acs.inorgchem.2c01743
Inorg. Chem. 2022, 61, 13442−13452

V.; Izmaylov, A. F.; Sonnenberg, J. L.; Williams-Young, D.; Ding, F.; Lipparini, F.; Egidi, F.; Goings, J.; Peng, B.; Petrone, A.; Henderson, T.; Ranasinghe, D.; Zakrzewski, V. G.; Gao, J.; Rega, N.; Zheng, G.; Liang, W.; Hada, M.; Ehara, M.; Toyota, K.; Fukuda, R.; Hasegawa, J.; Ishida, M.; Nakajima, T.; Honda, Y.; Kitao, O.; Nakai, H.; Vreven, T.; Throssell, K.; Montgomery, J. A., Jr.; Peralta, J. E.; Ogliaro, F.; Bearpark, M. J.; Heyd, J. J.; Brothers, E. N.; Kudin, K. N.; Staroverov, V. N.; Keith, T. A.; Kobayashi, R.; Normand, J.; Raghavachari, K.; Rendell, A. P.; Burant, J. C.; Iyengar, S. S.; Tomasi, J.; Cossi, M.; Millam, J. M.; Klene, M.; Adamo, C.; Cammi, R.; Ochterski, J. W.; Martin, R. L.; Morokuma, K.; Farkas, O.; Foresman, J. B.; Fox, D. J.. *Gaussian 16 Rev. A.03*; Wallingford, CT, 2016.

(60) Field, L. D.; George, A. V.; Malouf, E. Y.; Slip, I. H.; Hambley, T. W. Bis(acetylide) Complexes of Iron. *Organometallics* **1991**, *10*, 3842−3848.

(61) Manna, J.; John, K. D.; Hopkins, M. D. The Bonding of Metal-Alkynyl Complexes. *Adv. Organomet. Chem.* **1995**, *38*, 79−154.

(62) Toma, H. E.; Stadler, E.; Santos, P. S. Electronic and resonance Raman spectra of iron(II)-tetraazamacrocyclic complexes containing *N*-heterocyclic ligands. *Spectrochim. Acta, Part A* **1988**, *44*, 1365−1368.

(63) Dabrowiak, J. C.; Merrell, P. H.; Busch, D. H. High- and Low-Spin Six-Coordinate Complexes of Iron(II) with a Saturated Tetradentate Macrocyclic Ligand. *Inorg. Chem.* **1972**, *11*, 1979−1988.

(64) Dabrowiak, J. C.; Busch, D. H. Iron complexes with macrocyclic ligands containing the.alpha.-diimine functional unit and its position-specific formation under the influence of the iron atom. *Inorg. Chem.* **1975**, *14*, 1881−1888.

(65) Hay, R. W.; Lawrance, G. A.; Curtis, N. F. A Convenient Synthesis of the Tetra-aza-macrocyclic Ligands *trans*-[14]-Diene, Tet *a*, and Tet *b*. *J. Chem. Soc. Perkin Trans. 1* **1975**, 591−593.

(66) Chang, N.-H.; Mori, H.; Chen, X.-C.; Okuda, Y.; Okamoto, T.; Nishihara, Y. Synthesis of Substituted [6]Phenacenes through Suzuki-Miyaura Coupling of Polyhalobenzene with Alkenylboronates and Sequential Intramolecular Cyclization via C-H Bond Activation. *Chem. Lett.* **2013**, *42*, 1257−1259.

(67) Krejcik, M.; Danek, M.; Hartl, F. Simple construction of an infrared optically transparent thin-layer electrochemical cell: Applications to the redox reactions of ferrocene, Mn2(CO)10 and Mn(CO)3(3,5-di-t-butyl-catecholate). *J. Electroanal. Chem. Interfacial Electrochem.* **1991**, *317*, 179−187.

(68) Peverati, R.; Truhlar, D. G. An Improved and Broadly Accurate Approximation to the Exchange-Correlation Density Functional: The MN12-L Functional for Electronic Structure Calculations in Chemistry and Physics. *Phys. Chem. Chem. Phys.* **2012**, *14*, 13171−13174.

(69) Weigend, F.; Ahlrichs, R. Balanced basis sets of split valence, triple zeta valence and quadruple zeta valence quality for H to Rn: Design and assessment of accuracy. *Phys. Chem. Chem. Phys.* **2005**, *7*, 3297−3305.

(70) Tomasi, J.; Mennucci, B.; Cammi, R. Quantum mechanical continuum solvation models. *Chem. Rev.* **2005**, *105*, 2999−3093.

(71) Yu, H. S.; He, X.; Li, S. L.; Truhlar, D. G. MN15: A Kohn-Sham Global-Hybrid Exchange-Correlation Density Functional with Broad Accuracy for Multi-Reference and Single-Reference Systems and Noncovalent Interactions. *Chem. Sci.* **2016**, *7*, 5032−5051.

(72) Becke, A. D. Density-functional thermochemistry. III. The role of exact exchange. *J. Chem. Phys.* **1993**, *98*, 5648−5652.

(73) Grimme, S.; Antony, J.; Ehrlich, S.; Krieg, H. A consistent and accurate ab initio parameterization of density functional dispersion correction (DFT-D) for the 94 elements H-Pu. *J. Chem. Phys.* **2010**, *132*, No. 154104.

https://doi.org/10.1021/acs.inorgchem.2c01743
Inorg. Chem. 2022, 61, 13442−13452